Process Modeling of Aerosol-cloud Interaction in Summertime Precipitating Shallow Cumulus over the Western North Atlantic

Xiang-Yu Li[1], Hailong Wang[1], Matthew W. Christensen[1], Jingyi Chen[1], Shuaiqi Tang[1], Simon Kirschler[2], Ewan Crosbie[3,4], Luke D. Ziemba[3], David Painemal[3,4], Andrea F. Corral[5], Kayla Ann McCauley[6], Sanja Dmitrovic[7], Armin Sorooshian[5,6], Marta Fenn[3], Joseph S. Schlosser[5], Snorre Stamnes[3], Johnathan W. Hair[3], Brian Cairns[8], Richard Moore[3], Richard Anthony Ferrare[3], Michael A. Shook[3], Yonghoon Choi[3,4] Glenn S. Diskin[3], Joshua DiGangi[3], John B. Nowak[3], Claire Robinson[3,4], Taylor J. Shingler[3], Kenneth Lee Thornhill[3], Christiane Voigt[2]

[1]Pacific Northwest National Laboratory, Richland, WA, United States
[2]Institut für Physik der Atmosphäre, Deutsches Zentrum für Luft- und Raumfahrt (DLR), Oberpfaffenhofen, Germany, and Institute for Physics of the Atmosphere, Johannes Gutenberg-University Mainz, Germany
[3]NASA Langley Research Center, Hampton, VA, United States
[4]Analytical Mechanics Associates, Hampton, VA, United States
[5]University of Arizona, Department of Chemical and Environmental Engineering, Tucson, AZ, United States
[6]University of Arizona, Department of Hydrology and Atmospheric Sciences, Tucson, AZ, United States
[7]University of Arizona, James C. Wyant College of Optical Sciences, Tucson, AZ, United States
[8]NASA Goddard Institute for Space Studies, New York, NY, United States

Key Points:

- Aerosol-cloud interactions in precipitating shallow cumuli are investigated using large-eddy simulations (LES) and observations
- LES show that aerosol-induced cloud water adjustment is dominated by precipitation and is anticorrelated with cloud-top entrainment
- A decrease in cloud fraction in response to aerosol increase is shown in the precipitating cumuli

Corresponding author: Xiang-Yu Li, `xiangyu.li@pnnl.gov`

Corresponding author: Hailong Wang, `hailong.wang@pnnl.gov`

Abstract

Process modeling of aerosol-cloud interaction is essential to bridging gaps between observational analysis and climate modeling of aerosol effects in the Earth system and eventually reducing climate projection uncertainties. In this study, we examine aerosol-cloud interaction in summertime precipitating shallow cumuli observed during the Aerosol Cloud meTeorology Interactions oVer the western ATlantic Experiment (ACTIVATE). Aerosols and precipitating shallow cumuli were extensively observed with in-situ and remote-sensing instruments during two research flight cases on 02 June and 07 June, respectively, during the ACTIVATE summer 2021 deployment phase. We perform observational analysis and large-eddy simulation (LES) of aerosol effect on precipitating cumulus in these two cases. Given the measured aerosol size distributions and meteorological conditions, LES is able to reproduce the observed cloud properties by aircraft such as liquid water content (LWC), cloud droplet number concentration (N_c) and effective radius r_{eff}. However, it produces smaller liquid water path (LWP) and larger N_c compared to the satellite retrievals. Both 02 and 07 June cases are over warm waters of the Gulf Stream and have a cloud top height over 3 km, but the 07 June case is more polluted and has larger LWC. We find that the aerosol-induced LWP adjustment is dominated by precipitation and is anticorrelated with cloud-top entrainment for both cases. A negative cloud fraction adjustment due to an increase of aerosol number concentration is also shown in the simulations.

Plain Language Summary

Aerosol-cloud-interaction (ACI) regulates the energy budget of the Earth and poses the largest uncertainty in climate projection. Particularly, ACI of low clouds is poorly understood and causes the spread of Earth System Models (ESMs) in predicting cloud and climate responses to aerosol changes. Process studies have shown a nonlinear cloud water amount and cloud fraction adjustments due to aerosol changes via precipitation and cloud-top entrainment, which are not often captured correctly in ESMs. This study explores the physical mechanisms of ACI in marine low clouds with a focus on precipitating low clouds using a cloud process model and unprecedented field campaign measurements of meteorology states, cloud properties, and aerosols collected during the Aerosol Cloud meTeorology Interactions oVer the western ATlantic Experiment (ACTIVATE). We show that the aerosol-induced cloud water amount adjustment is dominated by changes in precipitation and is negatively correlated with cloud-top entrainment. Our findings can help improve the representation of ACI within precipitating marine low clouds in ESMs.

1 Introduction

Aerosol-cloud interaction (ACI) poses the largest uncertainty for accurate climate projection (Seinfeld et al., 2016). Assuming fixed liquid water path (LWP) and Cloud Fractional Coverage (CFC) increasing the aerosol number concentration N_a leads to a larger cloud droplet number concentration N_c, smaller effective radius r_{eff}, and stronger outgoing shortwave radiation (Twomey, 1977). The enhanced shortwave cloud radiative effect can affect the meteorological state and boundary layer structure of clouds (Li et al., 2023). Decreased r_{eff} suppresses the precipitation rate by inhibiting the collision-coalescence processes, resulting in a higher liquid water path (LWP) and possibly larger cloud fraction (Albrecht, 1989). This is the conventional wisdom of ACI involving multi-scale, nonlinear processes from aerosol/cloud microphysics to large-scale atmospheric circulations, which are fundamentally poorly understood due to the intractable scale range and strong nonlinearity, and therefore, mathematically poorly represented in Earth System Models (ESMs) (Seinfeld et al., 2016; Smith et al., 2020). Besides the strongly nonlinear nature of ACI, it is also in an emergent and non-equilibrium state, which hinders our understanding of processes that determines sinks and sources of aerosol and cloud. One example is the nonlinear interplay among N_a, N_c, and the sink terms of liquid water content (LWC) for summertime shallow cumuli (Seinfeld et al., 2016). The parameterization of these clouds is responsible for the spread of ESMs in estimating the equilibrium climate sensitivity (ECS) (Zhao et al., 2016). In addition, even though ACI of shallow cumuli was shown to affect the ECS (Gettelman et al., 2019), the magnitude is uncertain. Droplet evaporation and precipitation are the two major sinks of LWC. Larger N_a results in larger N_c but smaller cloud droplets, which are easier to evaporate. N_a-induced suppression of the precipitation rate leads to a positive LWP response (Glassmeier et al., 2021). Precipitation removes aerosols from clouds and therefore leads to a negative feedback on N_c (Radke et al., 1980). This LWP feedback is also influenced by aerosol hygroscopicity κ, which determines the activation rate of aerosols acting as cloud condensation nuclei (CCN) to form cloud droplets. κ poses a great challenge for ESMs due to uncertainties in the detailed composition of particles, aerosol mixing state, and potential nonlinear interactions between them (Petters & Kreidenweis, 2007).

The aforementioned aerosol-cloud-precipitation interaction is very challenging to simulate even using large-eddy simulations (LES), where the relevant large-size turbulent eddies for cloud formation are resolved but droplet-turbulence interactions are ignored. The latter (Li et al., 2020) enhances the collision-coalescence process that determines the precipitation rate. Ackerman et al. (2004) showed that LWP response to aerosol-induced precipitation suppression depends on the competition between moistening due to decreased surface precipitation and drying due to enhanced cloud-top entrainment. Therefore, the LWP adjustment in response to increasing N_a can be divided into entrainment-dominated and precipitation-dominated regimes. For non-precipitating clouds (typically having the appearance of closed cells), increasing N_a leads to more abundant, smaller cloud droplets that can evaporate more readily due to entrainment drying because smaller droplets provide a larger surface area for a fixed amount of LWP (Ackerman et al., 2004). This entrainment drying process leads to a negative LWP adjustment to increasing N_a, indicating less reflective clouds and therefore, a weaker cooling effect. For precipitating clouds (typically having the appearance of open cells), more abundant but smaller cloud droplets increase colloidal stability through the suppression of precipitation rate, and thus yield a larger value of LWP. This positive LWP adjustment to increasing N_a indicates thicker and more reflective clouds, i.e., a stronger shortwave radiative cooling effect (Albrecht, 1989). Satellite observations have suggested complex LWP adjustments. Gryspeerdt et al. (2019) showed a negative LWP adjustment in the majority of the oceanic regions using satellite retrievals, indicating that LWP reductions due to ACI could offset a significant fraction of the indirect aerosol radiative effect related to albedo increase. Diamond et al. (2020) reported significant cloud brightening due to increased N_a from ship emissions in subtropical low clouds, which is refuted by Glassmeier et al. (2021), who

pointed out that the shipping-induced aerosol radiative cooling for non-precipitating stratocumuli is overestimated by a factor of up to 200% because of the underestimated negative LWP adjustment related to current estimates of the average lifetimes of ship tracks. However, by considering both visible (as in Glassmeier et al. (2021)) and invisible ship tracks, Manshausen et al. (2022) showed positive LWP adjustment and therefore, a larger aerosol cooling effect. Aerosol effects on LWP and CFC based on satellite measurements only use snapshots of aerosol-cloud fields and ignore the temporal nature of cloud adjustments, which could lead to inaccurate estimation of aerosol effects (Bellouin et al., 2020). Recently, Arola et al. (2022) found that a positive LWP adjustment can be easily misinterpreted as a negative adjustment based on satellite measurements due to satellite retrieval errors (Painemal & Zuidema, 2011) and the propagation and spatial variability in aerosols and clouds that cannot be captured by satellite instruments. In addition, Christensen et al. (2022) concluded that these results from natural experiments cannot be easily scaled to global scales. This is because only shallow clouds are considered and the effect of emission on deeper clouds is omitted in natural experiments. Modeling studies (Wang et al., 2011; Possner et al., 2018) have shown that cloud brightening and LWP adjustments in response to aerosol emissions from ships depend strongly on boundary-layer meteorological conditions and dynamical feedback induced by precipitation change. This drives the need for an in-depth investigation of ACI in a more comprehensive meteorological context. The Aerosol Cloud meTeorology Interactions oVer the western ATlantic Experiment (ACTIVATE) field campaign (2020-2022) has been conducted to bridge such a gap.

Many studies focus on stratocumulus-to-cumulus cloud transitions, of which the physical drivers and feedbacks are still unclear (Sandu & Stevens, 2011). Wang & Feingold (2009) showed that precipitation change can drive the transition. Yamaguchi et al. (2017) and Wood et al. (2018) found fast transition ($\sim 10\,\mathrm{h}$) because of the drizzle initiation and depletion of aerosols by precipitation change using LES. A larger N_a elongates the timing of the transition even though it is modulated by the diurnal cycle and large-scale meteorology, as shown in the LES studies (Goren et al., 2019). Using satellite retrievals, Christensen et al. (2020) showed that aerosols enhance the lifetime of clouds and increase cloud fraction in stable atmospheric conditions during the stratocumulus-to-cumulus transition. Erfani et al. (2022) confirmed the delayed stratocumulus-to-cumulus-transition due to aerosol-cloud-precipitation interactions for initially clean MBL and Twomey effect for initially polluted MBL using LES with a prognostic aerosol model, where aerosol life cycle with sources and sinks of aerosols included.

In this study, we consider precipitating summertime cumuli observed during ACTIVATE since they can rapidly form rain (Rauber et al., 2007) and are an ideal candidate to study aerosol-cloud-precipitation interactions. In addition, the cloud fraction of these clouds are severely under-predicted (few percent) in the ESMs (Rémillard & Tselioudis, 2015; Sorooshian et al., 2019) compared to the satellite observations ($15-20\%$) in the North Atlantic region. We investigate the ACI of summertime cumuli over the Western North Atlantic Ocean (WNAO) region using LES and measurements during the ACTIVATE campaign. The ACTIVATE campaign aims to build unprecedented statistics to improve process-level understanding of ACI and their representation in ESMs (Sorooshian et al., 2019). To study aerosol-cloud-precipitation interactions, we select two contrasting cases from the ACTIVATE campaign. The first one is a clean case with heavy precipitation. The second one is a polluted case with light drizzling conditions. Contrary to most previous process studies that focused on sensitivity tests of ACI by arbitrarily perturbing the N_a or N_c (Wang & Feingold, 2009; Chen et al., 2011; Yamaguchi et al., 2017; Goren et al., 2019), we utilize measured N_a and N_c from ACTIVATE to understand ACI and its impact on LWP and CFC adjustments.
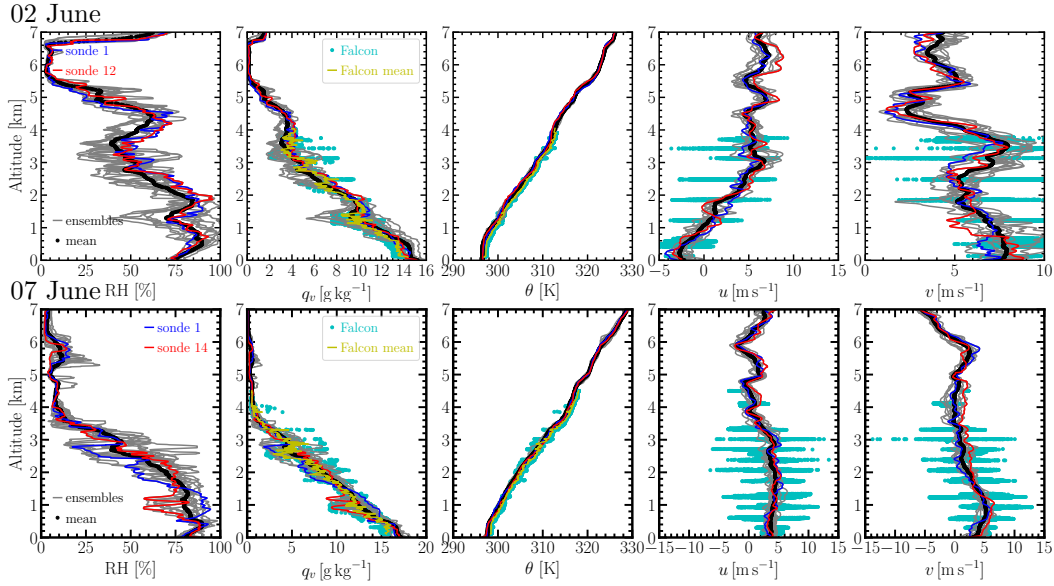
Figure 1. Profiles from dropsonde and Falcon measurements up to 7 km (same as the LES vertical domain size) for the 02 June (upper row) and 07 June (lower row) 2021 cases. The blue and red curves represent the first and last dropsonde, respectively, released at about the same location but one hour apart. The gray lines represent dropsondes in between, and the thick black lines represent the corresponding mean profile. The cyan dots show all the data points from the Falcon measurement (up to ~ 4 km) during the dropsonde measurement time. The yellow lines represent the averaged Falcon measurement every 10 m vertically to approximately match the vertical spacing of dropsonde profiles.

2 Data and methods

2.1 Observations and reanalysis data

2.1.1 Two precipitating cases

We select two contrasting process-study cases during the ACTIVATE 2021 summer field campaign. The case on 02 June 2021 is a heavily precipitating case (see the satellite visible image in Figure S1(a)) with the highest rain rate of $23\,\mathrm{mm\,h^{-1}}$ (the FCDP sampling frequency of 1 Hz) while the one on 07 June 2021 (Figure S1(b)) is a drizzling case (up to $5\,\mathrm{mm\,h^{-1}}$). The mean precipitation rate over the dropsonde circle is not provided due to the sample issue of the two-dimensional stereo (2DS) probe during the flight. However, the Fast Cloud Droplet Probe (FCDP)-r_{eff}, rain water path (RWP) produced by LES, and Falcon forward camera records support our categorization of the precipitation for these two cases. The ACTIVATE campaign employed a dual-aircraft strategy to provide spatially coordinated measurements of meteorology states, trace gases, aerosol, and cloud properties (Sorooshian et al., 2019, 2023). The high-flying ($\sim$9 km in altitude) King Air measures meteorology states using dropsondes (Li et al., 2022) as well as aerosol and cloud retrievals using remote sensing instruments. The low-flying Falcon conducts in-situ measurements of water vapor (Diskin et al., 2002), trace gases, aerosol, and cloud properties. Figure S2 and Figure S3 shows the vertical profiles of water vapor mixing ratio q_v at 12 dropsonde locations and the simultaneously measured N_c from the FCDP for the 02 and 07 June 2021 cases, respectively. The measurements took place between 18:29:20 to 19:46:16 UTC and 18:25:54 to 19:45:37 UTC for the 02 and 07 June 2021 cases, respectively.

2.1.2 Measured aerosol size distribution

A Scanning Mobility Particle Sizer (SMPS, TSI model 3085 differential mobility analyzer and TSI model 3776 condensation particle counter, 1/60 Hz) and a Laser Aerosol Spectrometer (LAS, TSI model 3340) were used to measure aerosol particles with diameter d between $3 - 100\,$nm and larger than $100\,$nm below the cloud base, respectively. Their uncertainty is within $\pm 10 - 20\%$ over the submicron aerosol size range (Moore et al., 2021). The measured aerosol size distributions are fitted with lognormal modes as shown in Figure S4(a) for the 02 June 2021 case and in Figure S4(b) for the 07 June 2021 case. The corresponding fitted parameters are listed in Table S1. The vertical structure of N_a is derived using combined polarimetric and lidar remote sensing observations (Schlosser et al., 2022). The retrieved vertical structure of N_a exhibits exponential decay with height (Figure S5). Our LES takes the lognormal distributions as aerosol input, which follows this exponential decay with height in the simulation domain.

2.1.3 Estimated hygroscopicity

The bulk hygroscopicity ($\bar{\kappa}$) of aerosol particles for each lognormal size mode is estimated from κ and mass of each chemical component m_i following the volume mixing rule (Petters & Kreidenweis, 2007). The m_i (listed in Table S2) is measured by an Aerodyne High Resolution Time-of-Flight Aerosol Mass Spectrometer (HR-ToF-AMS) (De-Carlo et al., 2008) with an uncertainty up to 50%. The estimated bulk hygroscopicity $\bar{\kappa}$ for aerosol particles larger than $60\,$nm in diameter d is listed in Table 1 and Table S3, which is used for the second and third mode of the lognormal distribution. For aerosol particles with $d \leq 60\,$nm (first mode of the lognormal distribution) that lack valid measurements, we use the smallest value of the organic component $\kappa = 0.014$ and the mean value $\kappa = 0.1$ for the 02 and 07 June 2021 cases, respectively. We adopt such treatment of estimating $\bar{\kappa}$ for two reasons. First, measuring mass fraction of aerosol particles with $d \leq 60\,$nm is very challenging with high uncertainties. Therefore, we use the estimated κ of the organic components from existing literature. Second, the smallest and mean κ value of the organic component as input yields the best matching cloud microphysical properties to the in-situ measurements for the 02 June and 07 June cases, respectively.

2.1.4 Measured cloud microphysical properties

The cloud droplet size distribution, N_c, and r_{eff} and LWC were measured by FCDP. The FCDP can measure cloud droplets with diameter ranging from $3 - 50\,\mu$m with an uncertainty of less than 20% (Baumgardner et al., 2017; Knop et al., 2021). Cloud particles larger than $50\,\mu$m are measured by the 2DS probe (Lawson et al., 2006) with a spatial resolution of $11.4\,\mu$m/pixel (Voigt et al., 2010; Bansmer et al., 2018). The 2DS covers a size range of $28.5 - 1464.9\,\mu$m in this study.

2.1.5 Reanalysis and satellite data

Since the idealized LES cannot capture the large-scale motions of the atmospheric flow, we use the fifth generation of European Centre for Medium-Range Weather Forecasts's Integrated Forecast System (ERA5) reanalysis (hourly model-level and single-level with a mesh grid-size of 31 km) large-scale forcings (i.e., moisture and temperature advective tendencies and wind profiles) and surface heat fluxes to drive the LES (Li et al., 2022, 2023). LWP retrieved from hourly single-level (quantities obtained from the model level) ERA5 and the Modern-Era Retrospective analysis for Research and Applications version 2 (MERRA-2) (starting from 00:30 UTC) is used for comparison with WRF-LES results and observations. The mean ERA5 (MERRA-2) LWP is calculated by averaging model grids over the dropsonde-covered area. Both ERA5 (hourly) and MERRA-2 (3-hourly) provide the CFC field at individual model levels, from which the time evolution of CFC is obtained by averaging the maximum values of the CFC vertical-profiles

obtained by sampling each layer conditionally with a threshold of LWC $= 0.02\,\mathrm{g\,cm^{-3}}$ for clouds below 7 km. Both LES and ERA5/MERRA-2 reanalysis results are compared to the GOES-16 product, the first of the GOES-R series of the Geostationary Operational Environmental Satellites (GOES). The GOES-16 cloud retrievals we use in this study have a pixel size of 2 km and a time interval of 20 minutes.

2.2 LES numerical experiment design

The Weather Research and Forecasting (WRF) model (Skamarock et al., 2019) in the idealized LES mode (WRF-LES), i.e., periodic boundary condition in horizontal directions (Wang et al., 2009), is used in this study. The LES domain has a lateral size of $L_x = L_y = 20\,\mathrm{km}$ with a grid spacing of $dx = dy = 100\,\mathrm{m}$ and a vertical extent of $z_{\mathrm{top}} = 7\,\mathrm{km}$ with 153 vertical layers. Although our sensitivity tests with $dx = dy = 300$ m produce deeper clouds (closer to the measurements) than the ones with $dx = dy = 100$ m (Figure S8 and Figure S11 in the supplement), we use a 100 m horizontal grid spacing to resolve smaller turbulent eddies that are important for the formation and evolution of shallow cumuli. Time-varying, area-averaged temperature and moisture advective tendencies ($\partial_t \bar{\theta}$ & $\partial_t \bar{q}_v$), divergence ($\bar{D}$), and surface turbulent heat fluxes are obtained from ERA5 for both cases except that the largest hourly surface heat fluxes among all the ERA5 grids within the dropsonde circle area are used for the 07 June 2021 case. A relaxation time scale of 3 hours is applied to nudge θ and q_v above 3 km and 1 hour for u and v in the entire domain to ERA5 for the 02 June 2021 case. This nudging strategy produces the best matching meteorology state (Figure S6 and Figure S7) to dropsonde measurements and observed cloud properties (Figure S8) to the FCDP measurements. For the 07 June 2021 case, only the u and v profiles are nudged to ERA5 with a time scale of 1 hour above 400 m and a 200 m transition depth to best reproduce the observed cloud properties. We adopt the Eulerian forcing instead of the Lagrangian one (forcing derived following the Lagrangian trajectory of the air mass) because the former leads to more comparable clouds to the observations (see the comparison between them in Figure S12–S14 in the supplement). The CAM radiative transfer model and a constant sea surface albedo of 0.06 are used. The Coriolis force corresponding to the center location of model domain is applied to all simulations.

The two-moment Morrison cloud microphysics scheme (Morrison et al., 2009) with prescribed aerosol size modes (see section 2.1.2) and hygroscopicity (see section 2.1.3) is employed, as initially implemented by Endo et al. (2015). Simulations with prescribed aerosol size distributions derived from the ACTIVATE campaign measurements, as described in section 2.1.2, are performed for both cases. We use prescribed aerosol size distribution instead of the prognostic one as in Erfani et al. (2022) because a prognostic aerosol model requires accurate information about particle and gas emissions to reproduce the observed aerosol size distributions. All simulations start at 06:00 UTC and end at 21:00 UTC with a fixed time step of 1 s. Initial profiles of temperature, humidity, and winds for all simulations are obtained from the corresponding ERA5 profiles averaged over the targeted case domain at 06:00 UTC. We refer to Table 1 for the input N_a, N_c, and $\bar{\kappa}$ of simulations.

3 Results

3.1 Aerosol effect on heavily precipitating cumuli: 02 June 2021 case

The 02 June 2021 case is characterized by heavy precipitation. The meteorology state from the dropsonde measurements exhibits strong spatial variation of RH (q_v) by comparing the grey curves (individual dropsondes) and black curve (mean profile) as shown in Figure 1(a). The strong spatial variation of q_v makes the simulation of this case challenging. The mean q_v-profile from the Falcon measurement (yellow curve) agrees with the dropsonde measurement. The instantaneous Falcon measurements (cyan dots) within

Table 1. List of simulations. "NC" denotes prescribed cloud droplet number concentration and "NA" denotes prescribed aerosol number concentration measured below cloud base.

Simulations	N_a^{input} [cm^{-3}]	N_c^{input} [cm^{-3}]	$\bar{\kappa}$
0602_NC	–	93	–
0602_NA	707	–	0.55
0607_NC	–	267	–
0607_NA	2073	–	0.35

the dropsonde circle for each case show strong spatiotemporal variations as well. The meteorology state from LES is evaluated against the dropsonde measurements. Compared to dropsonde measurements, both the 0602_NC and 0602_NA simulations yield colder θ and larger q_v below about 3.5 km and vice versa above, as shown in Figure 2(a) and (b). We then compare the cloud properties between LES and the FCDP measurements. Both simulations capture the measured LWC as shown in Figure 3(a) and the corresponding statistics in Figure S15(a). Simulation 0602_NA slightly overestimates (underestimates) N_c (r_{eff}) as shown in Figure 3(b) and (c) by comparing the red circles and black dots. Overall, our simulations capture the observed cloud properties reasonably well despite the aforementioned challenges.

To quantify the aerosol effect on precipitating cumuli, we adopt the metric of percentage difference (PD), defined as PD = $(\mathcal{Q}_{\text{NA}} - \mathcal{Q}_{\text{NC}})/\mathcal{Q}_{\text{NC}} \times 100\%$ with $\mathcal{Q}_{\text{NC}}$ and $\mathcal{Q}_{\text{NA}}$ representing quantities from the NC (baseline) and NA simulations, respectively (Li et al., 2023). $\mathcal{Q}$ is averaged between 08:00 and 20:00 UTC (Table S4). Simulation 0602_NA yields 52.7% larger (-6.6% smaller) N_c (r_{eff}) compared to 0602_NC as shown in Figure S16(e) and (f), suggesting a significant Twomey effect (Twomey, 1977). An increased N_c due to the aerosol loading suppresses the precipitation (the RWP is reduced by 38.9%) and leads to larger LWP (5.8%) as shown in Figure 4(a). This LWP adjustment is consistent with the findings in Albrecht (1989), which suggested that increasing cloud condensation nuclei (CCN) decreases the drizzle production and therefore increases the LWP for shallow marine clouds. CFC from simulation 0602_NA is larger until 16:00 UTC and then becomes smaller compared to 0602_NC (Figure 4(b)). In total, the aerosol loading leads to a 6.7% decrease of CFC , which is contrary to an increased CFC due to aerosol loading as suggested in Albrecht (1989). CFC increases and then decreases monotonically with RWP. The timing of the CFC peak is consistent with the one of RWP evolution (Figure S16). The shortwave cloud forcing at the top of the model decreases by $3.2\,\text{W}\,\text{m}^{-2}$ (a 4.4% decrease), suggesting a net aerosol cooling effect due to aerosol-cloud-precipitation interactions.

To quantify the aerosol effect on precipitation change, we examine the precipitation susceptibility defined as $S_o = -\Delta \ln R_p / \Delta \ln N_c$, where R_p is the precipitation rate. The rain frequency (E_p) susceptibility $-\Delta \ln \overline{E_p} / \Delta \ln \langle N_c \rangle$ is also examined. The precipitation susceptibility to aerosol perturbation depends on the LWP threshold (Sorooshian et al., 2009) and cloud thickness (Jung et al., 2016). R_p is least susceptible to N_c for weakly precipitating shallow MBL clouds because of low LWP ($\leq 500\,\text{g}\,\text{m}^{-2}$), is less susceptible to deeper convective BL clouds because of the large abundance ($\geq 1000\,\text{g}\,\text{m}^{-2}$) of LWP, and is most susceptible to MBL clouds with intermediate LWP ($\sim 500-1000\,\text{g}\,\text{m}^{-2}$). R_p from simulation 0602_NC (red dots with error bars) is larger than that from 0602_NA (cyan dots), as shown in Figure 5, because the prescribed aerosol loading leads to a larger N_c, smaller droplet size, and weaker precipitation rate. Consistent with the aerosol effect on R_p, the precipitation event E_p is also reduced in 0602_NA, as shown by the dashed curves in Figure 5. This aerosol-induced suppression of precipitation is further quantified by a positive value of S_o and $-\Delta \ln \overline{E_p} / \Delta \ln \langle N_c \rangle$ between NA and NC simulations
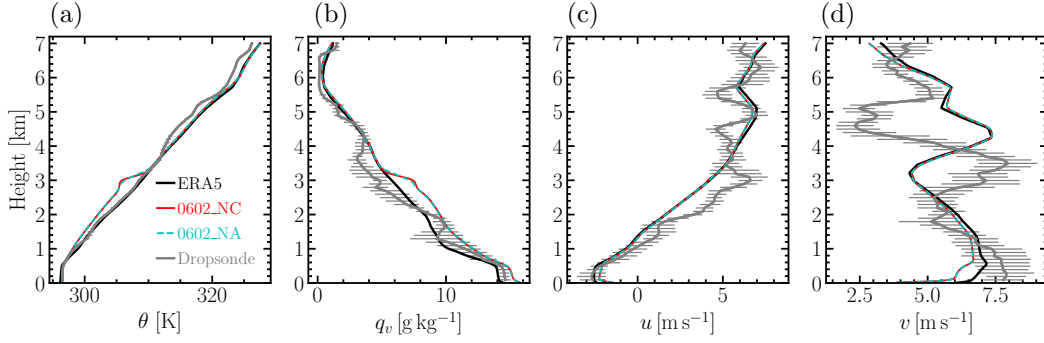
Figure 2. Domain-averaged vertical profiles from the WRF-LES simulation with the corresponding input forcings shown in Figure S23 at the measurement time for the 02 June 2021 case. The black line represents the ERA5 reanalysis data and the red (0602_NC) and cyan (0602_NA) ones represent the WRF-LES averaged values during the measurement time. The grey curves represent the dropsonde measurement with $\pm\sigma$ error bars.
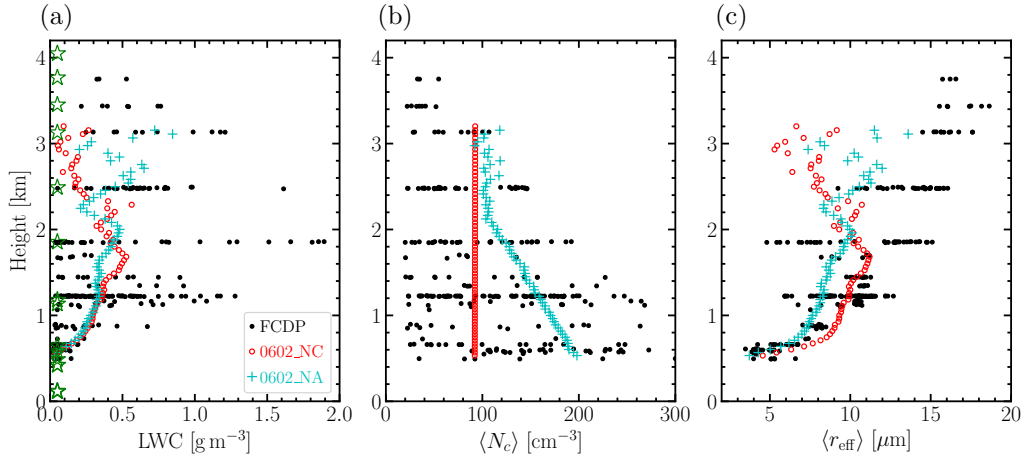

Figure 3. Comparison of vertical profiles of LWC, $\langle N_c \rangle$, and $\langle r_{\text{eff}} \rangle$ between the WRF-LES (0602_NC and 0602_NA listed in Table 1) and the FCDP measurements (black dots). A threshold of LWC $= 0.02\,\text{g}\,\text{m}^{-3}$, effective diameter $d_{\text{eff}} = 3.5\,\mu\text{m}$ and $N_c = 20\,\text{cm}^{-3}$ is applied to both the WRF-LES and the FCDP data. For the WRF-LES, only grid cells within clouds are averaged to obtain the vertical profile. The corresponding mean vertical profile of LWC, $\langle N_c \rangle$, and $\langle r_{\text{eff}} \rangle$ is obtained by averaging three snapshots of WRF-LES output (30 minutes apart). The green stars mark all flight legs above cloud base (ACB) and below cloud top (BCT).

shown in the penultimate column of Table 2, respectively. R_p from simulation 0602_NC (red dots with error bars) is larger than that from 0602_NA (cyan dots), as shown in Figure 5(a), because the prescribed aerosol loading leads to a larger N_c, smaller droplet size, and weaker precipitation rate. Consistent with the aerosol effect on R_p, the precipitation event E_p is also reduced in 0602_NA, as shown by the dashed curves in Figure 5(b). This aerosol-induced suppression of precipitation is further quantified by a positive value of S_o and $-\Delta \ln \overline{E_p}/\Delta \ln \overline{\langle N_c \rangle}$ between NA and NC simulations shown in the penultimate column of Table 2, respectively. The domain averaged LWP from our LES is less than $100\,\text{g}\,\text{m}^{-2}$ for both cases, which leads to a small mean rain rate and S_o (0.86 for the 02 June case). This is consistent with the findings in Sorooshian et al. (2009).
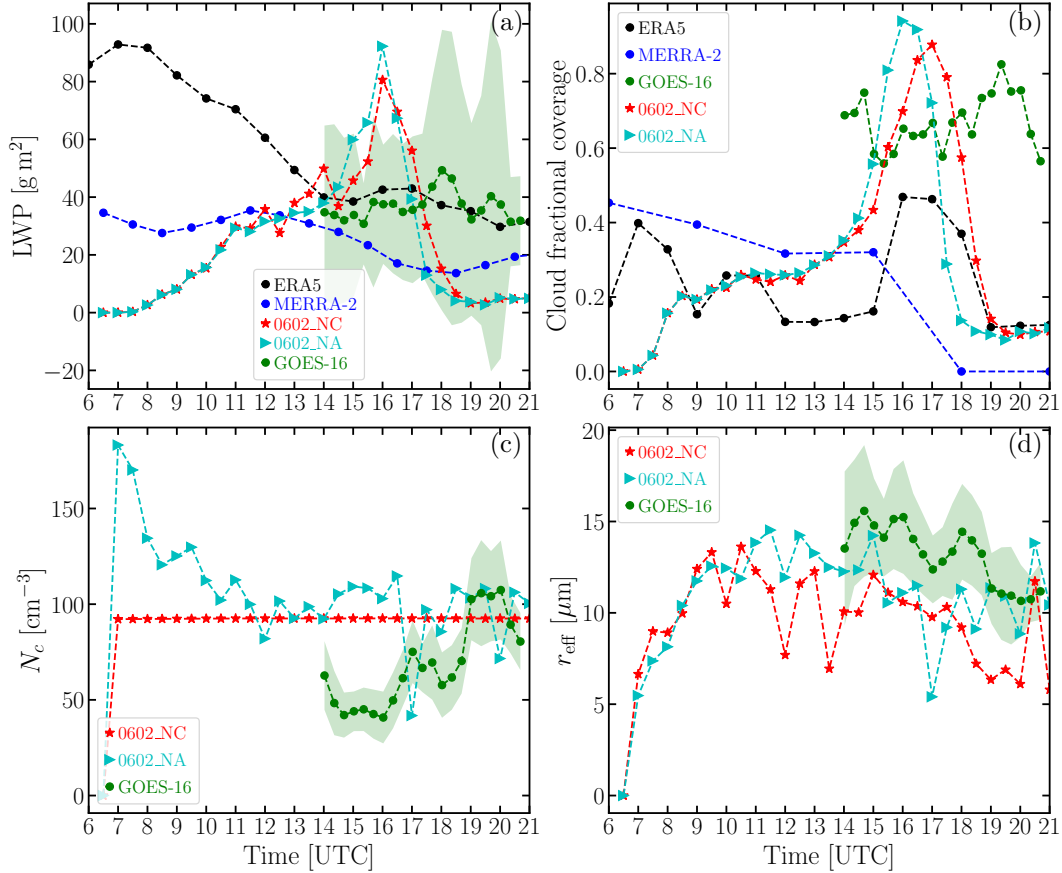
Figure 4. Comparison of cloud properties between the WRF-LES (0602_NC and 0602_NA in red and cyan, respectively), ERA5 (black), MERRA-2 (blue), and GOES-16 (green) for the 02 June 2021 case. The domain averaged LWP includes both cloud and rain water. N_c and r_{eff} are averaged (cloudy grid with LWC $\geq 0.02\,\text{g}\,\text{kg}^{-1}$) over the cloud top $(200 \quad - \quad 300\,\text{m})$ from the WRF-LES ouput. ERA5, MERRA-2, and GOES-16 data are averaged over the dropsonde area. The GOES-16 LWP, N_c, and r_{eff} data are filtered by a cloud optical depth threshold ≥ 3 to limit the systematic biases in LWP and r_{eff} following the procedure described in Painemal & Zuidema (2011) and Painemal et al. (2021).

3.2 Aerosol effect on drizzling cumuli: 07 June 2021 case

Compared to the 02 June 2021 case, the 07 June 2021 one is initially more polluted, in which N_a is about three times larger, as shown in the second column of Table 1. As a result, only drizzle was observed for the 07 June case. We first compare the vertical profiles (meteorology states) amongst the dropsonde measurement, LES, and ERA5 datasets. Both simulations, 0607_NC and 0607_NA, can reproduce the θ-profile compared to the dropsonde measurement, except for a warmer free troposphere between 4-6 km as shown in Figure 6(a). LES produces a more humid boundary layer until 2 km compared to the dropsonde measurements and ERA5, as shown in Figure 6(b). The LES horizontal wind components agree with the dropsonde measurements (Figure 6(e) and (f)). Overall, the LES captures the observed MBL meteorology states.

LES cloud microphsyical properties for this case are also evaluated against the FCDP measurements. Figure 7 shows that the measured LWC and N_c are very scattered, in-
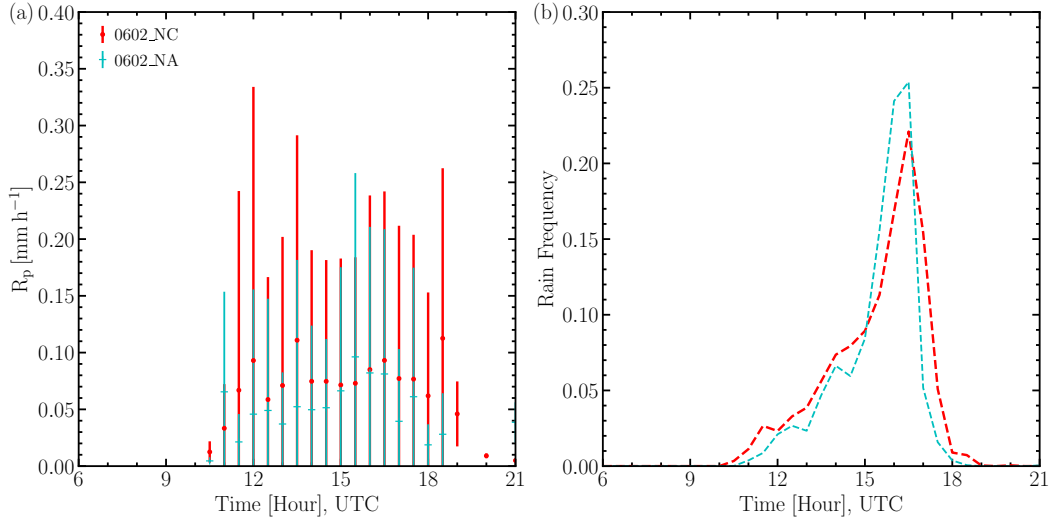
Figure 5. Precipitation rate (a) R_p (dots and pluses with error bars) and rain event frequency (b) E_p (dashed lines) for the 02 June 2021 case. A threshold of LWP $>$ $50\,\mathrm{g\,m^{-2}}$ and R_p $>$ $0.004\,\mathrm{mm\,h^{-1}}$ is applied to each grid to define rain events following Table 5 of Jiang et al. (2010). See Table 2 for the S_o calculation.

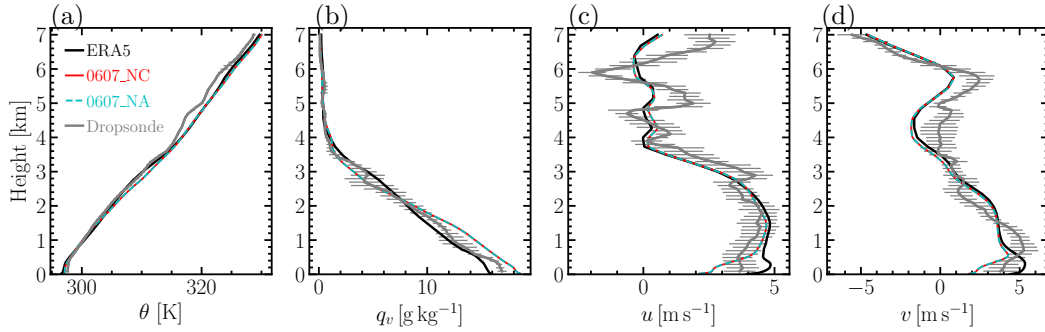**Figure 6.** Same as Figure 2 but for the 07 June case.

dicating a large spatial variability, but both simulations can reproduce the LWC and r_{eff} from the FCDP measurements well (see statistics in Figure S17).

After the evaluation of modeled meteorology state and cloud properties against the measurements, we now investigate the aerosol effect on drizzling (i.e., weakly precipitating) cumuli. Aerosol effect on LWP (PD $= -0.7\%$) and CFC (PD $= 1.6\%$) are almost negligible by comparing the time evolution of LWP and CFC for simulation 0607_NC (red stars) and 0607_NA (cyan triangles) as shown in Figure 8(a) and (b). This is likely because of the light precipitation, which is consistent with the wintertime ACTIVATE stratocumulus cases described in (Li et al., 2023). N_c (r_{eff}) from simulation 0607_NA is close to that from 0607_NC as shown in Figure S26(e) and (f). The impact of prescribed aerosols on the decrease in N_c (PD $= -31.6\%$) and the increase in r_{eff} (PD $= 12.9\%$) mostly reflects the Twomey effect. The aerosol induced RWP-reduction is 17.4%. The overall net cooling effect is $0.8\,\mathrm{W\,m^{-2}}$ (2.7%) in terms of short-wave (SW) cloud forcing at the top of the model.
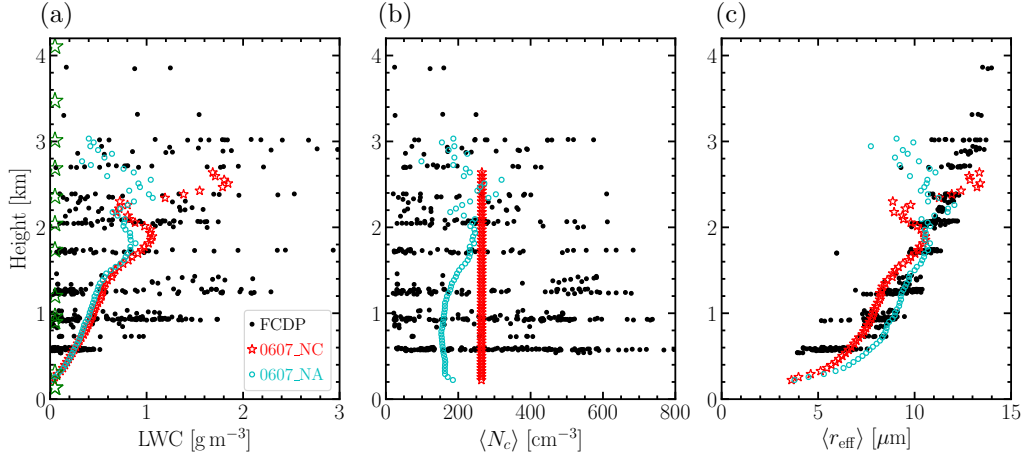
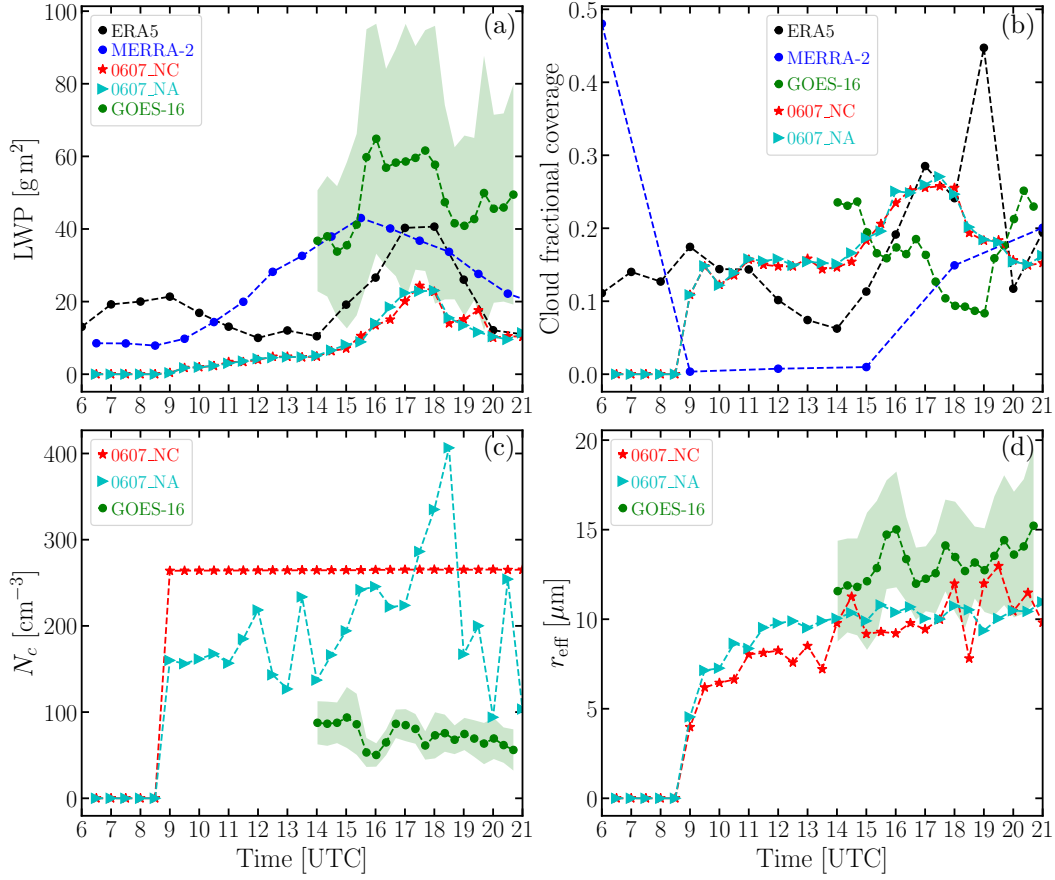**Figure 7.** Same as Figure 3 but for the 07 June case.

Figure 8. Same as Figure 4 but for the 07 June 2021 case. A comparison of the vertical profiles is shown in Figure 11.

3.3 Aerosol-induced LWP and CFC adjustment: entrainment and precipitation

As discussed in section 1, the LWP adjustment to aerosol-induced N_c, $\Delta \ln \overline{\mathrm{LWP}} / \Delta \ln \overline{\langle N_c \rangle}$, is nonlinear and depends on cloud regimes. In this section, we examine $\Delta \ln \overline{\mathrm{LWP}} / \Delta \ln \overline{\langle N_c \rangle}$

for the two cases studied here and contributing factors, i.e., precipitation and cloud-top entrainment. $\Delta \ln \overline{\text{LWP}}/\Delta \ln \overline{\langle N_c \rangle}$ is calculated by averaging the time series of LWP and $\langle N_c \rangle$ between 08:00 and 20:00 UTC. The positive value, 0.13 and 0.02 for the 02 June and 07 June case, respectively (Table 2), indicates precipitation-dominated LWP adjustments. The positive LWP adjustment leads to thicker and more reflective clouds. This is consistent with previous LES (Glassmeier et al., 2021) and satellite (Christensen et al., 2022) studies. We note that even though the 02 June case is clean and heavily precipitating and the 07 June one is polluted and lightly drizzling, the LWP adjustment due to aerosols are quite similar, suggesting that precipitation-dominated LWP adjustment, in response to the small aerosol or N_c perturbations, may not depend on the precipitation strength. The aerosol impact on cloud radiative effect can be quantified by the perturbation of cloud optical depth τ_c to N_c (Ghan et al., 2016),

$$\frac{\Delta \ln \overline{\tau_c}}{\Delta \ln \overline{\langle N_c \rangle}} = \frac{\Delta \ln \overline{\text{LWP}}}{\Delta \ln \overline{\langle N_c \rangle}} - \frac{\Delta \ln \overline{\langle r_{\text{eff}} \rangle}}{\Delta \ln \overline{\langle N_c \rangle}}. \tag{1}$$

Equation (1) shows that both the Twomey effect (second term) and the cloud macrophysical adjustment (first term) contribute to τ_c. For the 02 June case, the Twomey effect (0.2) and LWP adjustment (0.1) terms are comparable, which leads to a positive $\Delta \ln \overline{\tau_c}/\Delta \ln \overline{\langle N_c \rangle}$ of 0.3 (Table 1). For the 07 June case, the Twomey effect determines $\Delta \ln \overline{\tau_c}/\Delta \ln \overline{\langle N_c \rangle}$ and the LWP adjustment effect is negligible.

Entrainment is another important process contributing to cloud macrophysical adjustments. We first examine the 02 June 2021 case. w_e and LWP are anti-correlated with a Pearson correlation efficient of -0.39 (p-value=0.11) for simulation 0602_NC between 12:00-20:30 UTC (17 snapshots are used for the statistics) as shown in Figure 9(a). The same conclusion can be drawn for simulation 0602_NA but with a Pearson correlation efficient of -0.64 (p-value=0.005). w_e from simulation 0602_NC is slightly larger than that from 0602_NA as shown in Figure 9(b) from 16:30-17:30 UTC.

For the 07 June case, w_e is anti-correlated with LWP (Figure 9(c)) with a Pearson correlation coefficient of -0.45 (p-value = 0.06) and -0.56 (p-value = 0.01) for simulation 0607_NC and 0607_NA, respectively. This indicates that the cloud-top entrainment process has a pronounced effect on LWP for the drizzling cumuli, consistent with non-precipitating marine stratocumuli (Ackerman et al., 2004), where entrainment plays a significant role. The net shortwave radiative flux at the model top (not shown) shows moderate correlation with the w_e with a Pearson correlation coefficient of 0.66 (p-value = 0.003) and 0.69 (p-value = 0.001) for simulation 0607_NC and 0607_NA, respectively. The 0607_NC simulation yields slightly larger w_e from 16:30-17:30 UTC as can be seen from the time evolution of Δw_e (Figure 9(d)). Since the time-varying large-scale vertical velocity profile (based on ERA5 forcing) $\langle w \rangle_{z_i}$ is the same for the two simulations, Δw_e is due to the dz_i/dt, which is caused by the difference in cloud properties and consequent radiative impact on boundary layer structure for both cases.

3.4 Evaluation of large-scale models using LES

One of the goals of the present study is to evaluate the representation of cloud micro/macrophysics in large-scale models using LES and observations. ERA5 (black dots) agrees well with the GOES-16 measurements (green dots) in LWP while MERRA-2 (blue dots) shows smaller LWP in 14:00-21:00 UTC, as shown in Figure 4(a) for the 02 June 2021 case. CFC from ERA5 and MERRA-2 is smaller compared to GOES-16 (Figure 4(b)). The LES does not capture the spatial structure of LWP (Figure S18) or CFC (Figure 4(b)) compared to GOES-16. The LES N_c (r_{eff}) is larger (smaller) than GOES-16 as shown in Figure 4(c) and (d). However, we note that the GOES-16 N_c is smaller than FCDP–N_c during the FCDP measurement time (18:30-19:12 UTC). The time evolution of the domain averaged CFC from ERA5 (black dots) exhibits the same diurnal cycle as the LES (red stars and cyan triangles) (Figure 4(c)). However, compared to LES, ERA5 data exhibit
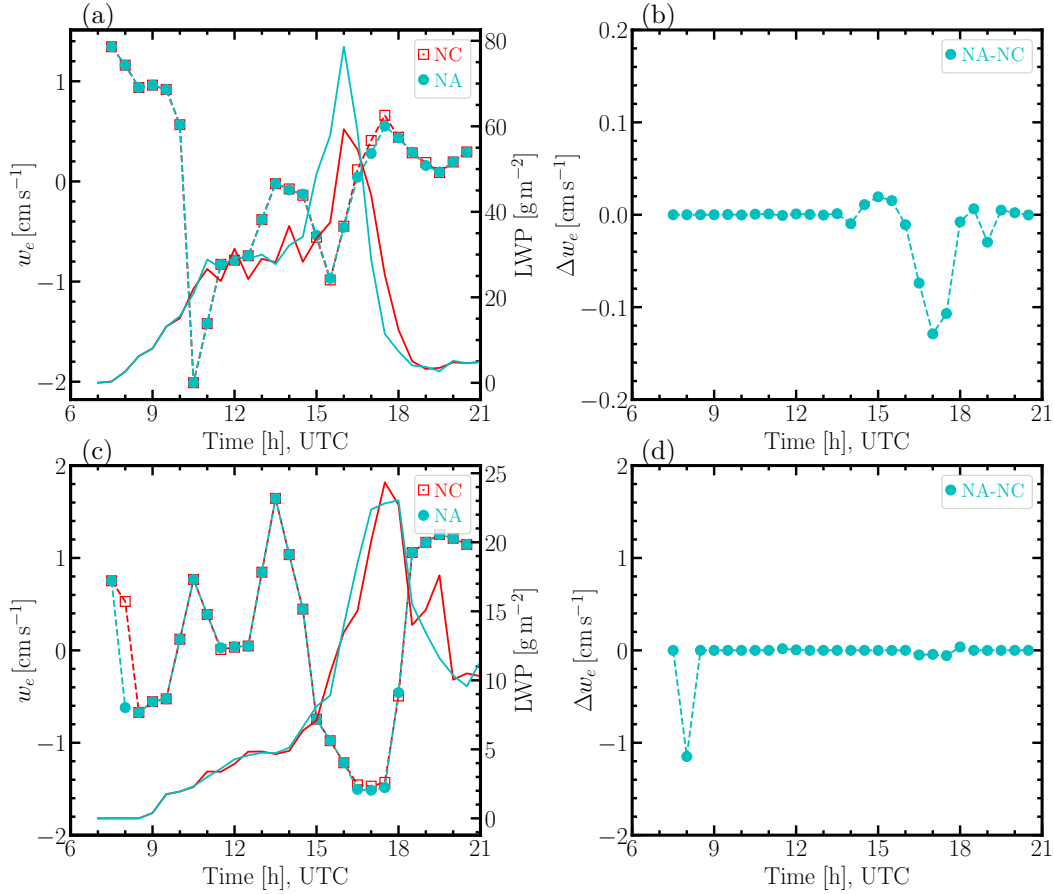
Figure 9. Entrainment rate $w_e = dz_i/dt - \langle w \rangle_{z_i}$ and the corresponding difference between NA and NC simulations Δw_e (squares) for the 02 ((a) and (b)) and 07 ((c) and (d)) June 2021 cases, where the cloud top height z_i is determined by the threshold LWC $\geq 0.02\,\mathrm{g\,kg^{-1}}$. $\langle w \rangle_{z_i}$ is the ERA5 large-scale vertical velocity at z_i. Solid lines in (a) and (c) represent the corresponding LWP.

higher clouds while MERRA-2 produces too low and little clouds as shown by the time evolution of CFC and LWC vertical profiles from the reanalysis data and LES in Figure 10.

  For the 07 June 2021 case, the LES (red stars and cyan triangles) produces $\sim 1/3$ LWP of GOES-16 (green symbols) during 14:00-21:00 UTC, as shown in Figure 8(a). The LES does not reproduce the GOES-16 LWP as shown in Figure S19. The CFC from LES is larger than that from GOES-16 (Figure 8(b)). The ERA5 LWP (black symbols) follows the same diurnal cycle as LES (red stars and cyan triangles) even though the magnitude is 2 times larger in 12:00-21:00 UTC (Figure 8(b)). This is remarkable considering the fact that cumuli hardly reach any steady state compared to the stratocumuli and that the ERA5 grid-spacing (30 km) is 300 times coarser than the LES (100 m). MERRA-2 (blue dots) has higher LWP than LES and ERA5. Neither the vertical structure of the ERA5 nor the MERRA2 LWC resembles the ones from LES (Figure 11(d)-(e)). The cloud vertical extent from ERA5 (Figure 11(d)) reaches 3 km between 09:00-12:00 UTC and 6 km around 18:00 UTC compared to 2 km from the LES (Figure 11(e)). The ERA5 CFC agrees reasonably with the LES while the MERRA-2 CFC is smaller than LES as shown in Figure 8(b). However, neither the ERA5 nor MERRA2 capture
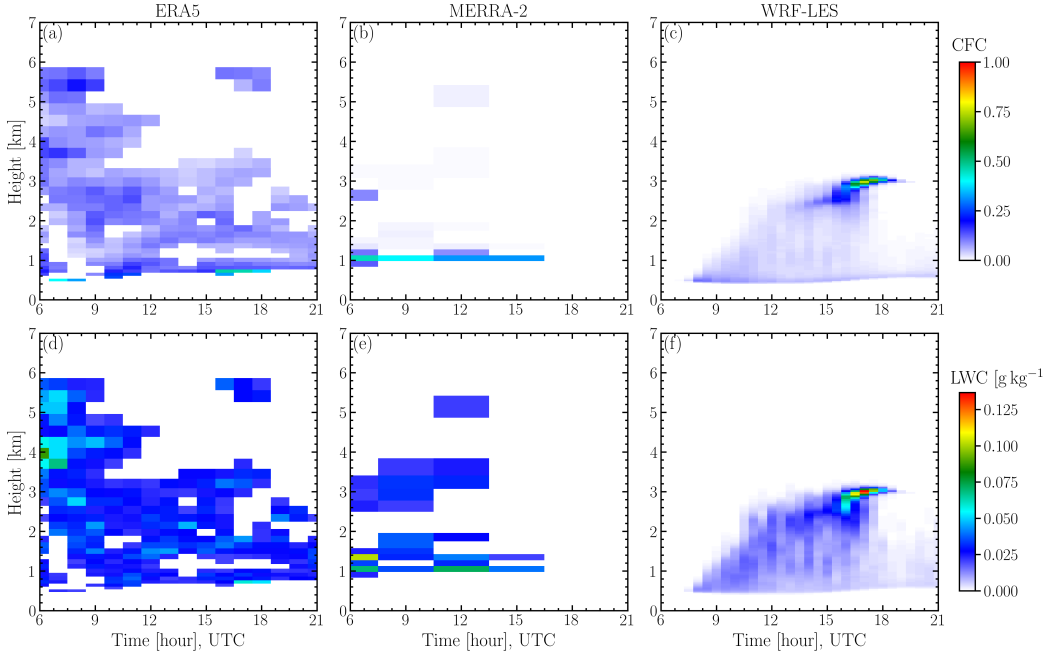
Figure 10. Evolution of vertical profile of CFC and LWC for the 02 June 2021 case. They are obtained by sampling each layer conditionally with a threshold of LWC $=$ $0.02\,\mathrm{g\,cm^{-3}}$. The 0602_NC vertical profiles are calculated by normalizing the cloudy grids with the total number of grids (200×200) at each model level. ERA5 and MERRA-2 data are averaged over the dropsonde circle area.

Table 2. Aerosol perturbation induced susceptibility of LWP and r_{eff} to N_c (cloudy average) between 08:00 and 20:00 UTC for the 02 and 07 June 2021 cases.

Case	$\Delta \ln \overline{\mathrm{LWP}}/\Delta \ln \overline{\langle N_c \rangle}$	$-\Delta \ln \overline{\langle r_{\mathrm{eff}} \rangle}/\Delta \ln \overline{\langle N_c \rangle}$	$\Delta \ln \overline{\tau_c}/\Delta \ln \overline{\langle N_c \rangle}$	$-\Delta \ln \overline{R_p}/\Delta \ln \overline{\langle N_c \rangle}$	$-\Delta \ln \overline{E_p}/\Delta \ln \overline{\langle N_c \rangle}$
02-06-2021	0.13	0.16	0.29	0.86	0.20
07-06-2021	0.02	0.32	0.34	–	–

the vertical structure of CFC compared to the LES (Figure 11(a)-(c)). We note that LES underestimates the observed cloud top height by about 1 km compared to in-situ measurements. This again demonstrates the challenge in simulating precipitating cumulus even using LES.

4 Discussions, conclusions, and outlook

We study aerosol-cloud-precipitation interactions in summertime precipitating shallow cumuli observed over the WNAO during the ACTIVATE campaign using LES. Two contrasting observational cases are selected. The 02 June 2021 case is a cleaner case featuring heavier precipitation, while the 07 June 2021 case is a more polluted one with lightly drizzling conditions. Both cases are very challenging to simulate due to the strong spatial variation of humidity and relatively deep boundary layer. For each case, the baseline LES is initiated with a constant droplet number concentration N_c from the ACTIVATE in-situ (FCDP) measurement. To perturb the LES clouds, we performed a sensitivity experiment with prescribed aerosol size distributions derived from SMPS/LAS
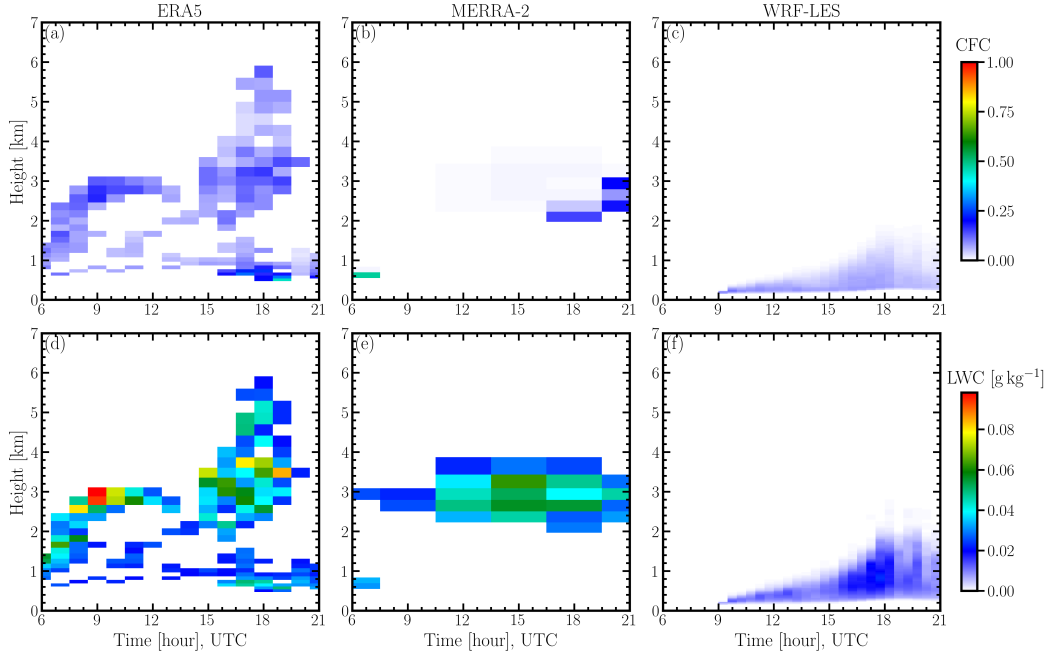
Figure 11. Same as Figure 10 but for the 07 June 2021 case.

measurements and the hygroscopicity κ derived from the AMS measurements. The LES experiments are forced by large-scale forcings, i.e., advective tendencies of θ and q_v and surface heat fluxes from ERA5 reanalysis data. The simultaneous measurements of the meteorology state and cloud properties allow us to evaluate our LES results at both small and large scales that are essential for understanding ACI. For the 02 June 2021 case, LES yields a slightly colder and more humid MBL compared to the dropsonde measurements. LES can reproduce the FCDP measurements of cloud microphysical properties, which agree reasonably well with the satellite retrievals. For the 07 June 2021 case, LES captures the θ profile well but produces a more humid MBL. The cloud microphysical properties (LWC, N_c, and r_{eff}) from LES agree with FCDP measurements. Overall, the LES is able to reproduce the measured cloud microphysics although the spatial variability is challenging to simulate. To capture the spatial variability, we perform simulations using ERA5 large-scale forcings at the location of individual dropsondes (see Figure S20–S22 in the supplement), none of which reproduce the observed clouds. This shows the challenge in simulating fast-evolving marine cumuli. The LES fails to reproduce the spatial structure of LWP compared to GOES-16 and does not agree well with the satellite microphysics retrievals, even though the LES reproduces the LWP compared to the Research Scanning Polarimeter (RSP) retrievals (Figure S25). The former could be because of the spatially uniform boundary conditions adopted in our LES that lack the mesoscale organizational structures shown in GOES-16 cloud field. The latter is likely due to both the idealized boundary conditions of the LES and uncertainties from the GOES-16 retrievals. The time evolution of LWP and CFC from ERA5 shows the same diurnal variation as LES for both cases although the fast-evolving subgrid shallow cumuli are challenging to simulate in ERA5 with much coarser spatio-temporal resolution than in LES.

For the clean and heavily precipitating case, LES predicts a a larger N_c, based on the observed aerosol size distribution and hygroscopicity, than the observed one, resulting in a suppression of precipitation and a larger LWP. This mechanism is consistent with many previous sensitivity studies of ACI. The CFC decreases as N_c increases despite an

increased LWP. To the best of our knowledge, it is the first time that this mechanism is tested in LES driven by measured cloud microphysics in the WNAO region. For the more polluted, lightly drizzling case, the aerosol loading predominately affects N_c and r_{eff} and has negligible effect on LWP and CFC, reflecting the Twomey effect alone. The LWP adjustment is dominated by precipitation change and is anti-correlated with the cloud-top entrainment rate for both cases.

The aerosol effect on precipitation rate is strongly nonlinear. The precipitation rate R_p has been argued to decrease with increasing aerosol number concentration N_a due to the suppression of collision-coalescence processes at fixed LWP in warm MBL (Albrecht, 1989). The assumption of a statistically steady LWP largely holds for stratocumuli (Glassmeier et al., 2021) but fails for the cumuli. This makes it challenging to quantify the precipitation susceptibility in cumuli. Positive precipitation susceptibility is observed for the heavily precipitating 02 June 2021 case due to the aerosol input that suppresses the precipitation. R_p is less susceptible to N_c for the lightly drizzling 07 June 2021 case. Our finding is consistent with previous studies of the R_p—N_a relationship for warm MBL clouds (Jung et al., 2016). Whether the aerosol effect on precipitation rate observed in the two cases here can be generalized to global scales remains to be investigated.

Acknowledgments

This work was supported through the ACTIVATE Earth Venture Suborbital-3 (EVS-3) investigation, which is funded by NASA's Earth Science Division and managed through the Earth System Science Pathfinder Program Office. The Pacific Northwest National Laboratory (PNNL) is operated for the U.S. Department of Energy by Battelle Memorial Institute under contract DE-AC05-76RLO1830. S.K. and C.V. were funded by the Deutsche Forschungsgemeinschaft (DFG, German Research Foundation) – TRR 301 – Project-ID 428312742.

Availability Statement

The source code used for the simulations of this study, the Weather Research and Forecasting (WRF) model, is freely available on `https://github.com/wrf-model/WRF`. The simulations were performed using resources available through Research Computing at PNNL. Model input and output files are available at `https://doi.org/10.5281/zenodo.8034149`. ACTIVATE observational data are publicly available at `https://asdc.larc.nasa.gov/project/ACTIVATE`. GOES-16 data can be obtained at `https://satcorps.larc.nasa.gov/prod/exp/activate/visst-pixel-netcdf/g16-sd/2021/`. ERA5 reanalysis data are available at `https://doi.org/10.24381/cds.adbb2d47`. MERRA-2 reanalysis data can be obtained at `https://disc.gsfc.nasa.gov/datasets?project=MERRA-2`.

References

Ackerman, A. S., Kirkpatrick, M. P., Stevens, D. E., & Toon, O. B. (2004). The impact of humidity above stratiform clouds on indirect aerosol climate forcing. *Nature*, *432*(7020), 1014–1017. Retrieved from `https://doi.org/10.1038/nature03174` doi: 10.1038/nature03174

Albrecht, B. A. (1989). Aerosols, Cloud Microphysics, and Fractional Cloudiness. *Science*, *245*(4923), 1227–1230. Retrieved from `https://www.science.org/doi/abs/10.1126/science.245.4923.1227` doi: 10.1126/science.245.4923.1227

Arola, A., Lipponen, A., Kolmonen, P., Virtanen, T. H., Bellouin, N., Grosvenor, D. P., ... Kokkola, H. (2022). Aerosol effects on clouds are concealed by natural cloud heterogeneity and satellite retrieval errors. *Nature Communications*, *13*(1), 7357. Retrieved from `https://doi.org/10.1038/s41467-022-34948-5` doi: 10.1038/s41467-022-34948-5

Bansmer, S. E., Baumert, A., Sattler, S., Knop, I., Leroy, D., Schwarzenboeck, A., ... Esposito, B. (2018, 6). Design, construction and commissioning of the Braunschweig Icing Wind Tunnel. *Atmospheric Measurement Techniques*, *11*(6), 3221–3249. Retrieved from `https://amt.copernicus.org/articles/11/3221/2018/` doi: 10.5194/amt-11-3221-2018

Baumgardner, D., Abel, S. J., Axisa, D., Cotton, R., Crosier, J., Field, P., ... Um, J. (2017, 1). Cloud Ice Properties: In Situ Measurement Challenges. *Meteorological Monographs*, *58*(1), 1–9. Retrieved from `https://journals.ametsoc.org/doi/10.1175/AMSMONOGRAPHS-D-16-0011.1` doi: 10.1175/AMSMONOGRAPHS-D-16-0011.1

Bellouin, N., Quaas, J., Gryspeerdt, E., Kinne, S., Stier, P., Watson-Parris, D., ... Stevens, B. (2020). Bounding Global Aerosol Radiative Forcing of Climate Change. *Reviews of Geophysics*, *58*(1), e2019RG000660. Retrieved from `https://agupubs.onlinelibrary.wiley.com/doi/abs/10.1029/2019RG000660` doi: https://doi.org/10.1029/2019RG000660

Chen, Y.-C., Xue, L., Lebo, Z. J., Wang, H., Rasmussen, R. M., & Seinfeld, J. H. (2011, 9). A comprehensive numerical study of aerosol-cloud-precipitation interactions in marine stratocumulus. *Atmospheric Chemistry and Physics*, *11*(18), 9749–9769. Retrieved from `https://acp.copernicus.org/articles/11/9749/2011/` doi: 10.5194/acp-11-9749-2011

Christensen, M. W., Gettelman, A., Cermak, J., Dagan, G., Diamond, M., Douglas, A., ... Yuan, T. (2022, 1). Opportunistic experiments to constrain aerosol effective radiative forcing. *Atmospheric Chemistry and Physics*, *22*(1), 641–674. Retrieved from `https://acp.copernicus.org/articles/22/641/2022/` doi: 10.5194/acp-22-641-2022

Christensen, M. W., Jones, W. K., & Stier, P. (2020). Aerosols enhance cloud lifetime and brightness along the stratus-to-cumulus transition. *Proceedings of the National Academy of Sciences*, *117*(30), 17591–17598. Retrieved from `https://www.pnas.org/doi/abs/10.1073/pnas.1921231117` doi: 10.1073/pnas.1921231117

DeCarlo, P. F., Dunlea, E. J., Kimmel, J. R., Aiken, A. C., Sueper, D., Crounse, J., ... Jimenez, J. L. (2008, 7). Fast airborne aerosol size and chemistry measurements above Mexico City and Central Mexico during the MILAGRO campaign. *Atmospheric Chemistry and Physics*, *8*(14), 4027–4048. Retrieved from `https://acp.copernicus.org/articles/8/4027/2008/` doi: 10.5194/acp-8-4027-2008

Diamond, M. S., Director, H. M., Eastman, R., Possner, A., & Wood, R. (2020). Substantial Cloud Brightening From Shipping in Subtropical Low Clouds. *AGU Advances*, *1*(1), e2019AV000111. Retrieved from `https://agupubs.onlinelibrary.wiley.com/doi/abs/10.1029/2019AV000111` doi: https://doi.org/10.1029/2019AV000111

Diskin, G. S., Podolske, J. R., Sachse, G. W., & Slate, T. A. (2002, 9). Open-path airborne tunable diode laser hygrometer. In *Diode lasers and applications in atmospheric sensing* (Vol. 4817, pp. 196–204). International Society for Optics and Photonics. Retrieved from `https://www.spiedigitallibrary.org/conference-proceedings-of-spie/4817/0000/Open-path-airborne-tunable-diode-laser-hygrometer/10.1117/12.453736.short` doi: 10.1117/12.453736

Endo, S., Fridlind, A. M., Lin, W., Vogelmann, A. M., Toto, T., Ackerman, A. S., . . . Liu, Y. (2015). RACORO continental boundary layer cloud investigations: 2. Large-eddy simulations of cumulus clouds and evaluation with in situ and ground-based observations. *Journal of Geophysical Research: Atmospheres*, *120*(12), 5993–6014. Retrieved from `https://agupubs.onlinelibrary.wiley.com/doi/abs/10.1002/2014JD022525` doi: https://doi.org/10.1002/2014JD022525

Erfani, E., Blossey, P., Wood, R., Mohrmann, J., Doherty, S. J., Wyant, M., & O, K.-T. (2022, 11). Simulating Aerosol Lifecycle Impacts on the Subtropical Stratocumulus-to-Cumulus Transition Using Large-Eddy Simulations. *Journal of Geophysical Research: Atmospheres*, *127*(21), e2022JD037258. Retrieved from `https://doi.org/10.1029/2022JD037258` doi: https://doi.org/10.1029/2022JD037258

Gettelman, A., Hannay, C., Bacmeister, J. T., Neale, R. B., Pendergrass, A. G., Danabasoglu, G., . . . Mills, M. J. (2019, 7). High Climate Sensitivity in the Community Earth System Model Version 2 (CESM2). *Geophysical Research Letters*, *46*(14), 8329–8337. Retrieved from `https://doi.org/10.1029/2019GL083978` doi: https://doi.org/10.1029/2019GL083978

Ghan, S., Wang, M., Zhang, S., Ferrachat, S., Gettelman, A., Griesfeller, J., . . . Zhang, K. (2016). Challenges in constraining anthropogenic aerosol effects on cloud radiative forcing using present-day spatiotemporal variability. *Proceedings of the National Academy of Sciences*, *113*(21), 5804–5811. Retrieved from `https://www.pnas.org/doi/abs/10.1073/pnas.1514036113` doi: 10.1073/pnas.1514036113

Glassmeier, F., Hoffmann, F., Johnson, J. S., Yamaguchi, T., Carslaw, K. S., & Feingold, G. (2021). Aerosol-cloud-climate cooling overestimated by ship-track data. *Science*, *371*(6528), 485–489. Retrieved from `https://www.science.org/doi/abs/10.1126/science.abd3980` doi: 10.1126/science.abd3980

Goren, T., Kazil, J., Hoffmann, F., Yamaguchi, T., & Feingold, G. (2019). Anthropogenic Air Pollution Delays Marine Stratocumulus Breakup to Open Cells. *Geophysical Research Letters*, *46*(23), 14135–14144. Retrieved from `https://agupubs.onlinelibrary.wiley.com/doi/abs/10.1029/2019GL085412` doi: https://doi.org/10.1029/2019GL085412

Gryspeerdt, E., Goren, T., Sourdeval, O., Quaas, J., Mülmenstädt, J., Dipu, S., . . . Christensen, M. (2019, 4). Constraining the aerosol influence on cloud liquid water path. *Atmospheric Chemistry and Physics*, *19*(8), 5331–5347. Retrieved from `https://acp.copernicus.org/articles/19/5331/2019/` doi: 10.5194/acp-19-5331-2019

Jiang, H., Feingold, G., & Sorooshian, A. (2010, 11). Effect of Aerosol on the Susceptibility and Efficiency of Precipitation in Warm Trade Cumulus Clouds. *Journal of the Atmospheric Sciences*, *67*(11), 3525–3540. Retrieved from `https://journals.ametsoc.org/doi/10.1175/2010JAS3484.1` doi: 10.1175/2010JAS3484.1

Jung, E., Albrecht, B. A., Sorooshian, A., Zuidema, P., & Jonsson, H. H. (2016, 9). Precipitation susceptibility in marine stratocumulus and shallow cumulus from airborne measurements. *Atmospheric Chemistry and Physics*, *16*(17), 11395–11413. Retrieved from `https://acp.copernicus.org/articles/16/11395/2016/` doi: 10.5194/acp-16-11395-2016

Knop, I., Bansmer, S. E., Hahn, V., & Voigt, C. (2021). Comparison of different droplet measurement techniques in the Braunschweig Icing Wind Tunnel. *Atmo-*

spheric Measurement Techniques, *14*(2), 1761–1781. Retrieved from `https://amt` `.copernicus.org/articles/14/1761/2021/` doi: 10.5194/amt-14-1761-2021

Lawson, R. P., O'Connor, D., Zmarzly, P., Weaver, K., Baker, B., Mo, Q., & Jonsson, H. (2006, 11). The 2D-S (Stereo) Probe: Design and Preliminary Tests of a New Airborne, High-Speed, High-Resolution Particle Imaging Probe. *Journal of Atmospheric and Oceanic Technology*, *23*(11), 1462–1477. Retrieved from `http://journals.ametsoc.org/doi/10.1175/JTECH1927.1` doi: 10.1175/JTECH1927.1

Li, X.-Y., Brandenburg, A., Svensson, G., Haugen, N. E. L., Mehlig, B., & Rogachevskii, I. (2020). Condensational and Collisional Growth of Cloud Droplets in a Turbulent Environment. *Journal of the Atmospheric Sciences*, *77*(1), 337–353. Retrieved from `https://journals.ametsoc.org/view/journals/atsc/77/1/` `jas-d-19-0107.1.xml` doi: https://doi.org/10.1175/JAS-D-19-0107.1

Li, X.-Y., Wang, H., Chen, J., Endo, S., George, G., Cairns, B., . . . Zuidema, P. (2022, 1). Large-Eddy Simulations of Marine Boundary Layer Clouds Associated with Cold-Air Outbreaks during the ACTIVATE Campaign. Part I: Case Setup and Sensitivities to Large-Scale Forcings. *Journal of the Atmospheric Sciences*, *79*(1), 73–100. Retrieved from `https://journals.ametsoc.org/view/journals/` `atsc/79/1/JAS-D-21-0123.1.xml` doi: 10.1175/JAS-D-21-0123.1

Li, X.-Y., Wang, H., Chen, J., Endo, S., Kirschler, S., Voigt, C., . . . Zeng, X. (2023, 1). Large-Eddy Simulations of Marine Boundary-Layer Clouds Associated with Cold-Air Outbreaks During the ACTIVATE Campaign. Part II: Aerosol–Meteorology–Cloud Interaction. *Journal of the Atmospheric Sciences*, *80*(4), 1025–1045. Retrieved from `https://journals.ametsoc.org/` `view/journals/atsc/aop/JAS-D-21-0324.1/JAS-D-21-0324.1.xml` doi: 10.1175/JAS-D-21-0324.1

Manshausen, P., Watson-Parris, D., Christensen, M. W., Jalkanen, J.-P., & Stier, P. (2022). Invisible ship tracks show large cloud sensitivity to aerosol. *Nature*, *610*(7930), 101–106. Retrieved from `https://doi.org/10.1038/` `s41586-022-05122-0` doi: 10.1038/s41586-022-05122-0

Moore, R. H., Wiggins, E. B., Ahern, A. T., Zimmerman, S., Montgomery, L., Campuzano Jost, P., . . . Wang, J. (2021, 6). Sizing response of the Ultra-High Sensitivity Aerosol Spectrometer (UHSAS) and Laser Aerosol Spectrometer (LAS) to changes in submicron aerosol composition and refractive index. *Atmospheric Measurement Techniques*, *14*(6), 4517–4542. Retrieved from `https://amt.copernicus.org/articles/14/4517/2021/` doi: 10.5194/amt-14-4517-2021

Morrison, H., Thompson, G., & Tatarskii, V. (2009, 3). Impact of Cloud Microphysics on the Development of Trailing Stratiform Precipitation in a Simulated Squall Line: Comparison of One- and Two-Moment Schemes. *Monthly Weather Review*, *137*(3), 991–1007. Retrieved from `http://journals.ametsoc.org/doi/` `10.1175/2008MWR2556.1` doi: 10.1175/2008MWR2556.1

Painemal, D., Spangenberg, D., Smith Jr., W. L., Minnis, P., Cairns, B., Moore, R. H., . . . Ziemba, L. (2021, 10). Evaluation of satellite retrievals of liquid clouds from the GOES-13 imager and MODIS over the midlatitude North Atlantic during the NAAMES campaign. *Atmospheric Measurement Techniques*, *14*(10), 6633–6646. Retrieved from `https://amt.copernicus.org/articles/14/6633/` `2021/` doi: 10.5194/amt-14-6633-2021

Painemal, D., & Zuidema, P. (2011, 12). Assessment of MODIS cloud effective radius and optical thickness retrievals over the Southeast Pacific with VOCALS-REx in situ measurements. *Journal of Geophysical Research: Atmospheres*, *116*(D24), n/a-n/a. Retrieved from `http://doi.wiley.com/10.1029/2011JD016155` doi: 10.1029/2011JD016155

Petters, M. D., & Kreidenweis, S. M. (2007, 4). A single parameter representation of hygroscopic growth and cloud condensation nucleus activity. *Atmo-*

spheric Chemistry and Physics, *7*(8), 1961–1971. Retrieved from `https://acp.copernicus.org/articles/7/1961/2007/` doi: 10.5194/acp-7-1961-2007

Possner, A., Wang, H., Wood, R., Caldeira, K., & Ackerman, T. P. (2018, 12). The efficacy of aerosol–cloud radiative perturbations from near-surface emissions in deep open-cell stratocumuli. *Atmospheric Chemistry and Physics*, *18*(23), 17475–17488. Retrieved from `https://acp.copernicus.org/articles/18/17475/2018/` doi: 10.5194/acp-18-17475-2018

Radke, L. F., Hobbs, P. V., & Eltgroth, M. W. (1980, 6). Scavenging of Aerosol Particles by Precipitation. *Journal of Applied Meteorology*, *19*(6), 715–722. Retrieved from `http://journals.ametsoc.org/doi/10.1175/1520-0450(1980)019<0715:SOAPBP>2.0.CO;2` doi: 10.1175/1520-0450(1980)019⟨0715:SOAPBP⟩2.0.CO;2

Rauber, R. M., Stevens, B., Ochs, H. T., Knight, C., Albrecht, B. A., Blythe, A. M., . . . Zuidema, P. (2007, 12). Rain in shallow cumulus over the ocean: The RICO campaign. *Bulletin of the American Meteorological Society*, *88*(12), 1912–1928. doi: 10.1175/BAMS-88-12-1912

Rémillard, J., & Tselioudis, G. (2015). Cloud Regime Variability over the Azores and Its Application to Climate Model Evaluation. *Journal of Climate*, *28*(24), 9707–9720. Retrieved from `https://journals.ametsoc.org/view/journals/clim/28/24/jcli-d-15-0066.1.xml` doi: https://doi.org/10.1175/JCLI-D-15-0066.1

Sandu, I., & Stevens, B. (2011, 9). On the Factors Modulating the Stratocumulus to Cumulus Transitions. *Journal of the Atmospheric Sciences*, *68*(9), 1865–1881. Retrieved from `https://journals.ametsoc.org/doi/10.1175/2011JAS3614.1` doi: 10.1175/2011JAS3614.1

Schlosser, J. S., Stamnes, S., Burton, S. P., Cairns, B., Crosbie, E., Van Diedenhoven, B., . . . Sorooshian, A. (2022). Polarimeter + Lidar–Derived Aerosol Particle Number Concentration. *Frontiers in Remote Sensing*, *3*. Retrieved from `https://www.frontiersin.org/articles/10.3389/frsen.2022.885332` doi: 10.3389/frsen.2022.885332

Seinfeld, J. H., Bretherton, C., Carslaw, K. S., Coe, H., DeMott, P. J., Dunlea, E. J., . . . Wood, R. (2016). Improving our fundamental understanding of the role of aerosol-cloud interactions in the climate system. *Proceedings of the National Academy of Sciences*, *113*(21), 5781–5790. Retrieved from `https://www.pnas.org/doi/abs/10.1073/pnas.1514043113` doi: 10.1073/pnas.1514043113

Skamarock, W. C., Klemp, J. B., Dudhia, J., Gill, D. O., Liu, Z., Berner, J., . . . others (2019). A description of the advanced research WRF model version 4. *National Center for Atmospheric Research: Boulder, CO, USA*, *145*(145), 550.

Smith, C. J., Kramer, R. J., Myhre, G., Alterskjær, K., Collins, W., Sima, A., . . . Forster, P. M. (2020, 8). Effective radiative forcing and adjustments in CMIP6 models. *Atmospheric Chemistry and Physics*, *20*(16), 9591–9618. Retrieved from `https://acp.copernicus.org/articles/20/9591/2020/` doi: 10.5194/acp-20-9591-2020

Sorooshian, A., Alexandrov, M. D., Bell, A. D., Bennett, R., Betito, G., Burton, S. P., . . . Zuidema, P. (2023). Spatially-coordinated airborne data and complementary products for aerosol, gas, cloud, and meteorological studies: The NASA ACTIVATE dataset. *Earth System Science Data Discussions*, *2023*, 1–79. Retrieved from `https://essd.copernicus.org/preprints/essd-2023-109/` doi: 10.5194/essd-2023-109

Sorooshian, A., Anderson, B., Bauer, S. E., Braun, R. A., Cairns, B., Crosbie, E., . . . Zuidema, P. (2019). Aerosol–cloud–meteorology interaction airborne field investigations: Using lessons learned from the U.S. West coast in the design of activate off the U.S. East Coast. *Bulletin of the American Meteorological Society*, *100*(8). doi: 10.1175/BAMS-D-18-0100.1

Sorooshian, A., Feingold, G., Lebsock, M. D., Jiang, H., & Stephens, G. L.   (2009).   On the precipitation susceptibility of clouds to aerosol perturbations. *Geophysical Research Letters*, *36*(13). doi: 10.1029/2009GL038993

Twomey, S.   (1977, 7).   The Influence of Pollution on the Shortwave Albedo of Clouds. *Journal of the Atmospheric Sciences*, *34*(7), 1149–1152.   Retrieved from `http://journals.ametsoc.org/doi/10.1175/1520-0469(1977)034<1149:TIOPOT>2.0.CO;2` doi: 10.1175/1520-0469(1977)034⟨1149:TIOPOT⟩2.0.CO;2

Voigt, C., Schumann, U., Jurkat, T., Schäuble, D., Schlager, H., Petzold, A., . . . Dörnbrack, A.   (2010, 9).   In-situ observations of young contrails – overview and selected results from the CONCERT campaign. *Atmospheric Chemistry and Physics*, *10*(18), 9039–9056.   Retrieved from `https://acp.copernicus.org/articles/10/9039/2010/` doi: 10.5194/acp-10-9039-2010

Wang, H., & Feingold, G.   (2009, 11).   Modeling Mesoscale Cellular Structures and Drizzle in Marine Stratocumulus. Part I: Impact of Drizzle on the Formation and Evolution of Open Cells. *Journal of the Atmospheric Sciences*, *66*(11), 3237–3256. Retrieved from `https://journals.ametsoc.org/doi/10.1175/2009JAS3022.1` doi: 10.1175/2009JAS3022.1

Wang, H., Rasch, P. J., & Feingold, G.   (2011, 5).   Manipulating marine stratocumulus cloud amount and albedo: a process-modelling study of aerosol-cloud-precipitation interactions in response to injection of cloud condensation nuclei. *Atmospheric Chemistry and Physics*, *11*(9), 4237–4249.   Retrieved from `https://acp.copernicus.org/articles/11/4237/2011/`   doi: 10.5194/acp-11-4237-2011

Wang, H., Skamarock, W. C., & Feingold, G. (2009). Evaluation of Scalar Advection Schemes in the Advanced Research WRF Model Using Large-Eddy Simulations of Aerosol–Cloud Interactions. *Monthly Weather Review*, *137*(8), 2547–2558. Retrieved from `https://journals.ametsoc.org/view/journals/mwre/137/8/2009mwr2820.1.xml` doi: https://doi.org/10.1175/2009MWR2820.1

Wood, R., O, K.-T., Bretherton, C. S., Mohrmann, J., Albrecht, B. A., Zuidema, P., . . . Minnis, P.   (2018, 5).   Ultraclean Layers and Optically Thin Clouds in the Stratocumulus-to-Cumulus Transition. Part I: Observations. *Journal of the Atmospheric Sciences*, *75*(5), 1631–1652.   Retrieved from `https://journals.ametsoc.org/doi/10.1175/JAS-D-17-0213.1` doi: 10.1175/JAS-D-17-0213.1

Yamaguchi, T., Feingold, G., & Kazil, J. (2017). Stratocumulus to Cumulus Transition by Drizzle. *Journal of Advances in Modeling Earth Systems*, *9*(6), 2333–2349. Retrieved from `https://agupubs.onlinelibrary.wiley.com/doi/abs/10.1002/2017MS001104` doi: https://doi.org/10.1002/2017MS001104

Zhao, M., Golaz, J.-C., Held, I. M., Ramaswamy, V., Lin, S.-J., Ming, Y., . . . Guo, H. (2016). Uncertainty in Model Climate Sensitivity Traced to Representations of Cumulus Precipitation Microphysics. *Journal of Climate*, *29*(2), 543–560. Retrieved from `https://journals.ametsoc.org/view/journals/clim/29/2/jcli-d-15-0191.1.xml` doi: https://doi.org/10.1175/JCLI-D-15-0191.1